MARSHALL
GRANT
IN-76-CR
71414
P_38

FIFTH SEMI-ANNUAL PROGRESS REPORT

NASA GRANT NAG8-790

PROCESS MODELLING FOR MATERIALS PREPARATION EXPERIMENTS

Period of Performance
8/1/91 through 1/31/92

Principal Investigator

FRANZ ROSENBERGER

Co-Principal Investigators

J. IWAN D. ALEXANDER

(NASA-CR-189904) PROCESS MODELLING FOR MATERIALS PREPARATION EXPERIMENTS Semiannual Progress Report No. 5, 1 Aug. 1991 - 31 Jan. 1992 (Alabama Univ.) 38 p CSCL 20B

N92-19106

Unclas

G3/76 0071414

Center for Microgravity and Materials Research
University of Alabama in Huntsville
Huntsville, Alabama 35899

Table of Contents

1. Introduction and General Status

The main goals of the research under this grant consist of the development of mathematical tools and measurement of transport properties necessary for high fidelity modelling of crystal growth from the melt and solution, in particular for the Bridgman-Stockbarger growth of mercury cadmium telluride (MCT) and the solution growth of triglycine sulphate (TGS). The tasks, desribed in detail in the original proposal, include:

- development of a spectral code for moving boundary problems,
- kinematic viscosity measurements on liquid MCT at temperatures close to the (composition dependent) melting point, and
- diffusivity measurements on concentrated and supersaturated TGS solutions.

The work performed during the fifth six-monthly period of this grant has closely followed the schedule of tasks.

The code development has progressed well, though some difficulties have been encountered during this period, which are related to the rate of convergence of our spectral method. Efforts to remedy this have begun.

The oscillating-vessel technique that we developed for the measurement of the kinematic viscosity of melts at high temperatures and pressures, has been tested with water and gallium. Excellent agreement with literature values was obtained. Hence, the technique will be applied to MCT in the final reporting period.

For diffusivity measurements in (aqueous) solutions we have developed and tested a technique that overcomes some of the limitations of earlier techniques. During this report period we have performed extensive tests with concentrated NaCl solutions. Good agreement with published diffusivity data was obtained. Measurements with TGS will be performed in the final reporting period.

In the following we will give detailed descriptions of the work performed for these tasks, together with a summary of the resulting publications and presentations.

2. MCT Viscosity Measurements.

A detailed evaluation of the capillary type viscometer for measurements of HgCdTe melts was performed during the previous reporting period. Two principal difficulties have been identified:

1. Larger than expected quantities of material (>500g) are needed in order to build up a hydrostatic pressure head sufficient to suppress unwanted surface tension effects, such as the formation of bubbles in the capillary;

2. The assessment of safe cell dimensions for high pressure operation is difficult due to the complexity of the glassware used in this technique.

2.1. New Experimental Technique : Oscillating-cup Viscometry

To circumvent the above shortcomings a complementary technique based on the oscillation principle was to be developed. The important advantage of this technique is the possibility to use a simple sealed silica cell with a small quantity of material. Two such sealed ampules with $Hg_{0.8}Cd_{0.2}T$ were supplied by Texas Instruments. Hence, we do not have to become involved in the preparation of HgCdTe preparation, which would require appropriate facilities. In addition, the safety margin with HgCdTe melts in thick-walled silica ampules is considerably higher, than in the corresponding capillary method. However, as disadvantages of the oscillating-cell or -cup technique one should mention the complexity of instrumentation and data analysis.

In this reporting period, an oscillating-cup or -cell viscometer suitable for viscosity measurements of HgCdTe melts has been designed, fabricated, assembled and tested.

The principle of the oscillating-cup method is based on the damping effect of a contained liquid on the oscillatory motion of the container. The energy of the torsional pendulum is successively dissipating due to the viscous acceleration and deceleration of the liquid. Thus, the time dependence of the angular deflection can be written as

$$\alpha(t) = A \exp(-\frac{\delta t}{T}) \cos(\omega t + \varphi) \;,$$

where the angular frequency $\omega = 2\pi/T$, with T the period of the damped oscillation. The viscosity of the liquid can be calculated from the measured logarithmic decrement δ and the frequency of the oscillation. In addition, the dimensions and density of the liquid, the moment of inertia and the logarithmic decrement of the empty suspended system are required for the evaluation

The most reliable and practical equation for viscosity determination with cylindrical oscillating-cup viscometers is the formula derived by Roscoe (1958)

$$\mu = \left(\frac{I\delta}{\pi R^3 H Z}\right)^2 \frac{1}{\pi \rho T}$$

where

$$Z = \left(1 + \frac{R}{4H}\right) a_0 - \left(\frac{3}{2} + \frac{4R}{\pi H}\right)\frac{1}{p} + \left(\frac{3}{8} + \frac{9R}{4H}\right)\frac{a_2}{2p^2}$$

$$p = \left(\frac{\pi\rho}{\mu T}\right)^{1/2} R$$

$$a_0 = 1 - \frac{1}{2}\Delta - \frac{3}{8}\Delta^2$$

$$a_2 = 1 + \frac{1}{2}\Delta + \frac{1}{8}\Delta^2$$

$$\Delta = \frac{\delta}{2\pi}.$$

The parameters in these relations are as follows: I is the moment of inertia of the suspended empty oscillating system, ρ is the density of the liquid, T is the period of oscillations, R is the inner radius of the cylindrical cell, H is the height of the liquid in the cell, η is the viscosity of the liquid and δ is the logarithmic decrement of the empty torsional pendulum. The above set of equations has to be solved numerically for the viscosity. Means of determining the moment of inertia I will be described below.

A schematic view of the developed viscometer is presented in Fig.1. Basically, it consists of a torsional oscillation system enclosed in vacuum. A hardened steel (piano) wire of 0.01" diameter is suspended from a strain gauge bridge, which, in turn, is suspended from a shaft that is inserted through a vacuum feedthrough from the outside. A hand knob at the end of this shaft permits manual induction of an oscillation. At the bottom end, the wire is attached to a flywheel assembley. This assembley consists of an inertia disk with exchangeable rings. A silica suspension connects the flywheel to a sealed silica cell for the liquid. A vacuum system (turbomolecular and rotary pumps) can provide a vacuum of the order of 10^{-5} Torr in order to eliminate damping of the oscillations due to friction with air. The furnace used can be controlled with 0.1 ^{o}C resolution from "ambient" to 1300 ^{o}C. Three independently controlled heater zones allow for the adjustment of temperature uniformity of ± 2°C over the length of the silica cell.

Optical techniques are commonly used for measurements of oscillations. In a standard setup, a laser beam, deflected from a mirror attached to the oscillating assembley is projected onto a semicircular scale. The amplitude of the oscillation can be determined visually or, alternatively, recorded with a photoconductive linear displacement detector. Instead, we are recording the torsional amplitude with a simple strain gauge arrangement, and collect and process the data in a PC.

Figure 2 depicts the torsional motion sensing arrangement. Four strain gauges (Omega HBM 6/350 LY 11) are glued to the four top stainless steel foil springs of the cross-patterned metal strip basket. The torsional deformation of the wire over the length of the basket is coupled to the foil springs through the four horizontal spokes of the basket. During the oscillations, these foil springs are slightly bent, resulting in a signal from the strain gauges in a bridge arrangement with a strain gauge amplifier (Omega model DMD). This particular arrangement is rather selective with respect to torsional oscillations and suppresses signals from horizontal oscillations.

In order to determine a moment of inertia I of the suspended system, the torque constant G of the suspended system and its period of oscillation T needs to be measured. Then I can be calculated from the relation

$$I = G\left(\frac{T}{2\pi}\right)^2 = G\,\omega^{-2}\,.$$

In order determine G and its possible dependence on the suspended weight, we have performed oscillation experiments with 2 different inertial rings added to the flywheel:

Dimensions and mass of the first ring: R_1=34.42 mm, R_2=26.60 mm, m=152.4 g

Dimensions and mass of the second ring: R_1=34.30 mm, R_2=26.65 mm, m=261.0 g.

From the relation for the moment of inertia of a ring about its symmetry axis

$$I=m/2(R_1{}^2+R_2{}^2)\,,$$

we calculated

$$I_1=1442.2 \text{ gcm}^2 \quad \text{and} \quad I_2=2462.16 \text{ gcm}^2.$$

The measured angular frequencies were:

Measured frequencies:

no rings: w_0=1.77 s^{-1} ,
with the first ring attached: w_1=0.866 s^{-1},
with the second ring attached: w_2=0.699 s^{-1}.

From $I_0 = I_1\,\omega_1^2/(\omega_0^2 - \omega_1^2)$ and $I_0 = I_2\,\omega_2^2/(\omega_0^2 - \omega_2^2)$, we obtained $I_0 = 454$ gcm^2.

Furthermore, the three independently calculated values for the torpue constant were:

$G = 454*1.77^2$=1422.3gcm^2/sec^2, G=(454+1442.2)*0.866^2=1422.06gcm^2/sec^2 and G=(454+2462.16)*0.699^2=1424.8gcm^2/sec^2.

Since these values agree well with each other, we can assume that load effects can be ignored in the viscosity evaluation in our apparatus.

The sampling rate of the data aquisition system (DAS) was chosen to be 10/sec, which is sufficient for accurate recording of oscillations with periods in the range of 5-10 sec. Total data acquisition times of approximately 1 hour were used. The smallest oscillations which our detection system can still resolve is about 1 angular degree. Maximum angular amplitudes used were of the order of 90 degrees. We have carefully evaluated our data for possible nonlinear effects introduced by the detection system or the suspension wire. However, all data consistently showed strictly exponential decay of the amplitudes over more than two orders of magnitude; for details see below. In addition, the signals were quite sinusoidal with no detectable distorsions due to additional parasitic harmonics. The power spectra of the recorded signals showed only a single peak and a noise background of a constant magnitude. One third of the total signal trace of a typical experiment is presented in Fig.3.

Initially, the data were analyzed with a routine that calculated the local amplitudes of the oscillation as the difference between a local minimum and an adjacent local maximum. However, the resulting logarithmic plots of the decaying amplitudes showed often a deviation from a straight line in particular at lower amplitudes; see curve 1 in Fig. 4 obtained with water (see below). This could be indicative of nonlinear torsional movement, which, in fact, has been reported in the literature. Another possible cause is a low signal to noise ratio towards the end of the damped oscillation, were linear, pendulous oscillation contributions become relatively important. In order to filter the noise, a more complex analysis was performed by fitting a portion of the data (usually a couple of oscillations) to a sinusoidal function (nonlinear fitting with 4 parameters, a_0, a_1, ω, ϕ: $a_0 + a_1 \sin(\omega t+\phi)$). Amplitudes a_1 found this way are then plotted on a logarithmic scale. They exhibit no marked or systematic deviation from a straight line, as demonstrated by curve 2 in Fig. 4. Consequently, we concluded that no apparent nonlinear effects are present under our experimental conditions.

2.2. Low Temperature Measurements : Viscosity of Water

We have performed test measurement with water in a cell in air. The data were processed with Roscoe's formula. The following set of parameters were used : $\rho = 1$ g/cm^3, R = 1.1 cm, H = 16.5 cm, I = 1422*(1/0.9)^2 = 1755.6 gcm^2, T = 6.981 s, δ=0.0145. These resulted in η=0.00943 poise at 22.5 C, which is in excellent agreement with published data .

2.3. High Temperature Measurements: Viscosity of Molten Gallium.

A test experiment with molten gallium was performed to evaluate the heating arrangement. First, 100.05 g of gallium in form of pellets was loaded into the glass cell. Then, the logarithmic decrement was measured in air as well as in vacuum. The following values were obtained: in air: δ=0.00331; in vacuum δ=0.00222. After taking these measurements, the furnace was powered. In Fig. 5 one can clearly discern the moment when gallium began to melt. Measurements were made at various temperatures between 27 and 300 °C. Figures 6-8 show the plots of amlitudes versus time obtained at 200, 250 and 300 °C, respectively. The measurement at 200 ^{o}C was repeated once after a complete temperature cycle and gave the same result within 1% . For the viscosity calculations of gallium, the following data were used: $\omega = 0.855$ sec^{-1}, ρ = 6.1 g/cm^3, R = 1.1 cm, H = 4. 2cm, G = 1422 gcm^2/sec^2. The δ's obtained at the various temperatures, after subtraction of the intrinsic logarithmic decrement of the system (δ_{vac}) are listed in Table 1.

Table 1: Logarithmic decrements versus temperature obtained for gallium

Temperature [°C]	δ
27	0.01406
100	0.01227
150	0.01147
200	0.01125
250	0.01082
300	0.01036

The resulting viscosities are plotted in Fig. 9, together with literature data which, assuming Arrhenius behavior, follow the relation $\eta = 0.3567*10^{217.4/T}$ cp. While there is good agreement below 150 °C, there is a deviation of about 10% at the higher temperatures.

In conclusion, the equipment for viscosity measurements of molten HgCdTe was tested using water and liquid gallium. The overall performance is quite satisfactory. We expect to obtain viscosity data on HgCdTe system with an accuracy of at least 95%; the temperature slope of the viscosity, which is particularly important for theoretical evaluations can be expected to be resolved with even higher accuracy.

3. TGS Diffusivity Measurements

In earlier reports our approach to measuring the diffusion coefficients of supersaturated solutions was outlined. A rectangular optical cell is initially partly filled with a solution of a certain concentration C. A solution of higher concentration C + ΔC is then injected at the bottom of the cell with a syringe. The resulting system is convectively stable with the heavier solution below the lighter one and mixing occurs by diffusion only. A Zygo Mark II Mach-Zehnder interferometer interfaced with a personal computer is used to follow the evolution of the concentration profile in the cell. At regular intervals the interferometric intensity profiles produced are stored. The advanced fringe analysis software ZAPPC is then used to convert these into refractive index profiles which are proportional to the concentration. A numerical integration of these profiles, described in detail in the last progress report, yields the diffusivity.

In order to assume that the diffusivity D is a constant in the range of ΔC and keep the evaluation method numerically tractable, this concentration difference has to be small. Additionally, the supersaturated concentration region extends from the saturation point to the spinodal limit and this range is small for most solutions, usually well below 1M. For concentration measurements in this region ΔC has to be smaller than this range. These considerations suggest that it is preferable to maintain ΔC at 0.1M.

The effect that runs counter to this is the convection which is caused by the injection of the solution of concentration C+ΔC into the cell. When ΔC is large the density stratification in the cell is more stable and convection caused by injection subsides faster, producing less scatter in the data. Hence, in order to obtain good reproducibility the two competing effects had to be balanced. With a ΔC of 0.1M convection persists for longer times as the heavier solution now settles more slowly, with the resulting scatter in the data as high as 5%. To dampen convection without resorting to excessive values of ΔC, progressively thinner cells were employed. Our criterion was that the data should have scatter of less than 2% for a ΔC of 0.2M. In the last report results were given for cells of 1mm light path and they were still somewhat unsatisfactory. In the last few months new cells of smaller path lengths were used in an attempt to improve these results further. Cells of 0.2mm path length completely damped out convection but now the path length was so small that it was difficult to observe and measure the concentration differences interferometrically, that is the effective optical path lengths differences between various points in the cell were very small. Cells of 0.5mm path length gave a good balance between measurability and dampening of convection.

Unfortunately cells of less than 1mm path length are not manufactured in standard rectangular shape. Additionally, due to the difficulty of cleaning cells that thin, they are made with detachable covers and in our experiment this led to problems of seepage between the glass plates. Cells of 1mm path length inserted with microscope slides to reduce the path length were also tried and here again it was difficult to avoid seepage of the solution between the slides. All this meant that the process of obtaining good data had become very difficult and time consuming. At this point the decision was made to abandon the optical cells provided by cell manufacturers and design our own system.

3.1 New Interferometry Cell

An exploded presentation of the new demountable and readily cleanable cell is given in Fig. 10. The cell consists of two rectangular windows that sandwich a Viton gasket. Four bolts excert sufficient pressure onto the windows through two precision-machined brass flanges with highly planar faces to prevent any leakage. The windows consist of standard microscope slides that have been tested interferometrically. The solutions are injected through the open top and viewed through the windows in the flanges. The light path length is equal to the thickness of the rubber sheet and can be adjusted by using sheets of different thickness. The results reported below were obtained using rubber of 0.7mm thickness.

With this arrangement all the difficulties associated with this method, as reported earlier, have been overcome. Diffusivities of supersaturated solutions can now be measured with good reproducibility. An additional benefit is that only flat glass slides are used here, not glass cells which a have greater probability of having stress points. This lack of stress points in the glass produces fringe patterns of greater uniformity. All this is shown by the reproducibility of the data which is better than ±1.5%.

3.2 High Concentration NaCl Solutions

Before application of this technique to TGS, we have performed careful measurements with saturated and supersaturated solutions of NaCl, for which data are available ion the literature. Our results are summarized in Table 1. Note that the saturation point at 25 °C is 5.3

molar (M). The standard deviations shown are the result of six independent measurements for each data point.

Table 1. Measured Diffusivities of Concentrated NaCl solutions at 25 °C

Method Used	Diffusivities (cm^2/s)		
	5M	5.2M	5.4M
Previous work [1, 2 & 3]	1.584×10^{-5}	1.580×10^{-5}	1.49×10^{-5}
Light path=1mm, ΔC=0.15M	$(1.56\pm0.04)\times10^{-5}$		
Light path=1mm, ΔC=0.3M	$(1.57\pm0.02)\times10^{-5}$		
Light path=0.7mm, ΔC=0.2M	$(1.58\pm0.02)\times10^{-5}$	$(1.57\pm0.02)\times10^{-5}$	$(1.48\pm0.02)\times10^{-5}$

At this stage we can state that an accurate new interferometric method of measuring diffusion coefficients of saturated and supersaturated solutions has been developed. The only other attempt to measure diffusivities of supersaturated solutions was made by Myerson and co-workers [3]. Our method is not only simpler but provides better reproducibility than the ±3% achieved in [3]. Work on the diffusivities of supersaturated TGS solutions utilizing this technique will begin shortly.

References

[1] V. Vitagliano and P.A. Lyons, *Diffusion Coefficients for Aqueous Solutions of Sodium Chloride and Barium Chloride*, J. Amer. Chem. Soc., **78** (1956) 1549.

[2] J.A. Rard and D.G. Miller, *The Mutual Diffusion Coefficients of NaCl-H_2O and $CaCl_2$-H_2O at 25 °C from Rayleigh Interferometry*, J. Solution Chem, **8**(1979) 701.

[3] Y.C. Chang and A.S. Myerson, *The Diffusivity of Potassium Chloride and Sodium Chloride in Concentrated, Saturated and Supersaturated Solutions*, AIChE J., **31** (1985) 890.

4. MCT Code Development

4.1 Introduction

During the last semi-annual period work was completed on the solution of the moving boundary problem for axisymmetric solidification in the absence of convection. In addition, a code which solves for axisymmetric convective flow in a circular cylinder using a Chebyshev pseudo-spectral method together with an influence matrix method was also completed. The solidification code development is described in section **4.2** and the axisymmetric convection code is described in section **4.3**.

4.2 Solidification: Code Development

Governing equations and boundary conditions

The governing equations and boundary conditions are described in terms of a cylindrical coordinate system with the orgin located at the centerline and the top of the ampoule. Variables are put in dimensionless form by scaling lengths with the ampoule radius R and defining the dimensionless temperature as $T=(T^* - T_c)/(T_h - T_c)$ where $T_h - T_c$ is the (fixed) temperature difference between the top and bottom of the ampoule

$$\Delta T_m = Pe_m \frac{\partial T_m}{\partial z}, \tag{1}$$

$$\Delta T_c = Pe_c \frac{\partial T_c}{\partial z}, \tag{2}$$

$$\Delta T_a = Pe_a \frac{\partial T_a}{\partial z}, \tag{3}$$

where subscripts m, c, and a refer to melt, crystal and ampoule, respectively. Here, the Peclet number, $Pe = V_a R/\alpha$, represents the dimensionless transition rate of the ampoule, and V_a, R and α are, respectively, the growth velocity, ampoule radius and thermal diffusivity.

Boundary conditions

$$T(r, 0) = 1, \tag{4}$$

$$T(r, \Lambda) = 0, \tag{5}$$

$$\frac{\partial T(0, z)}{\partial r} = 0, \tag{6}$$

$$\frac{\partial T(R_W, z)}{\partial r} = Bi(T - T_f), \tag{7}$$

where $\Lambda = L/R$ is the aspect ratio of the ampoule, with L being the ampoule length, $R_w = (R + d_w)/R$ with d_w = ampoule wall thickness, Bi(z) is a dimensionless heat transfer coefficient defined to include radiative and convective heat transfer between the ampoule and the furnace, and $T_f(z)$ is the temperature distribution of the furnace wall.

At the melt/solid interface

$$-\left(\frac{\partial T}{\partial n}\right)_c + \frac{K_m}{K_c}\left(\frac{\partial T}{\partial n}\right)_m = \mathrm{Ste}\,\mathrm{Pe}(\mathbf{e}_z \cdot \mathbf{n})\,, \tag{8}$$

$$T = T^*\,, \tag{9}$$

where **n** is the unit vector normal to the interface, $\mathbf{e}_z$ is the unit vector in cylindrical coordinate and $\mathrm{Ste} = \Delta H/C_p\Delta T$ is the Stefan number and T^* is the dimensionless melting temperature of the crystal. Perfect thermal contact at the melt/ampoule and crystal/ampoule interface is assumed. Thus, the heat fluxes at these boundaries are equal i.e.

$$\left(\frac{\partial T}{\partial r}\right)_m = \frac{K_a}{K_m}\left(\frac{\partial T}{\partial r}\right)_a \text{ and } \left(\frac{\partial T}{\partial r}\right)_c = \frac{K_a}{K_c}\left(\frac{\partial T}{\partial r}\right)_a\,, \tag{10}$$

at $r = 1$.

Solution method

Nonorthogonal transformation

The nonorthogonal coordinate transformations utilized in this study (Fig. 11) are the following:

$$\text{Upper domain,} \quad \xi = r, \quad \eta = \frac{z}{h(r)}\,,$$

$$\text{Lower domain,} \quad \xi = r, \quad \eta = 2 - \frac{z - \Lambda}{h(r) - \Lambda}\,,$$

where h(r) is the melt/crystal interface position. In the ampoule, h(r)=h(R)=constant. The transformed governing equations now take the form

$$\frac{\partial^2 T}{\partial \xi^2} + A\frac{\partial^2 T}{\partial \eta^2} + B\frac{\partial^2 T}{\partial \eta \partial \xi} + C\frac{\partial T}{\partial \xi} + D\frac{\partial T}{\partial \eta} = 0\,, \tag{11}$$

where in the upper domain,

$$A = \frac{1}{h^2} + \left(\frac{\eta}{h}\frac{\partial h}{\partial r}\right)^2 ,$$

$$B = -\frac{2\eta}{h}\frac{\partial h}{\partial r} \qquad C = \frac{1}{\xi},$$

$$D = (2\left(\frac{1}{h}\frac{\partial h}{\partial r}\right)^2 - \frac{1}{h}\frac{\partial^2 h}{\partial r^2} - \frac{1}{\xi h}\frac{\partial h}{\partial r})\eta - \frac{Pe}{h}.$$

Here, Pe should be taken as Pe_m and Pe_a, respectively, for the melt and ampoule.

In the lower domain,

$$A = \frac{1}{(h-\Lambda)^2} + \left(\frac{\eta-2}{h-\Lambda}\frac{\partial h}{\partial r}\right)^2 ,$$

$$B = -\frac{2(\eta-2)}{h-\Lambda}\frac{\partial h}{\partial r} \qquad C = \frac{1}{\xi},$$

$$D = (2\left(\frac{1}{h-\Lambda}\frac{\partial h}{\partial r}\right)^2 - \frac{1}{h-\Lambda}\frac{\partial^2 h}{\partial r^2} - \frac{1}{\xi(h-\Lambda)}\frac{\partial h}{\partial r})(\eta-2) + \frac{Pe}{h-\Lambda},$$

where Pe should be taken as Pe_c and Pe_a respectively in the crystal and ampoule. The boundary conditions are also subject to the coordinate transformations.

Pseudospectral discretization

The total solution domain is divided into four subdomains (Fig.1) and for each subdomain the equation (11) is discretized using a Chebyshev-collocation method. The Chebyshev polynomial expansion for the dependent variables is

$$T = \sum_{\substack{i=1 \\ j=1}}^{M,N} c_{ij} t_i(x) t_j(y)), \tag{12}$$

where $t_i(x) = \cos(i\arccos(x))$, $t_j(y) = \cos(j \arccos y)$, and x and y are defined by the transformations given in Fig. 11 for each of the subdomains. The Gauss-Lobatto collocation points are

$$x_i = \cos\frac{\pi(i-1)}{M-1} \text{ and } y_j = \cos\frac{\pi(j-1)}{N-1}), \tag{13}$$

The Chebyshev collocation derivative of a function T(x,y) can be represented as

$$\left(\frac{\partial T}{\partial x}\right)_{ij} = \sum_{p=1}^{m} D_x^{ip} T(x_p, y_j) , \tag{14}$$

$$\left(\frac{\partial T}{\partial y}\right)_{ij} = \sum_{q=1}^{n} D_y^{jq} T(x_i, y_q) , \tag{15}$$

$$\left(\frac{\partial T}{\partial y}\right)_{ij} = \sum_{q=1}^{n} D_y^{jq} T(x_i, y_q) , \tag{15}$$

$$\left(\frac{\partial^2 T}{\partial y^2}\right)_{ij} = \sum_{q=1}^{n} D_{yy}^{jq} T(x_i, y_q) , \tag{17}$$

$$\left(\frac{\partial^2 T}{\partial x \partial y}\right)_{ij} = \sum_{\substack{p=1 \\ q=1}}^{m,n} D_x^{ip} D_y^{jq} T(x_p, y_q) , \tag{18}$$

where the expressions for D_x, D_y, D_{xx}, D_{yy} and D_{xy} are given by Ouazzani[1].For large m, n, the Chebyshev collocation differentiation can be efficiently implemented by using FFT's (Fast Fourier Transforms), which eliminates the use of expensive matrix multiplication involved with (14)-(18).

PGCR method for finite difference preconditioning

In the present investigation, the preconditioning solution method for spectral equations involves finite difference preconditioning imbedded within each iteration. This allows the problem to retain spectral accuracy while using a finite-difference method to solve a related auxiliary problem. For this purpose, we need a finite difference discretization for the preconditioned version of equation (11). The following second order accurate finite difference formulas are employed for the entire non-uniform grid:

$$\left(\frac{\partial f}{\partial x}\right)_i = \frac{dx_i}{dx_i + dx_{i+1}} \frac{f_{i+1} - f_i}{dx_{i+1}} + \frac{dx_{i+1}}{dx_i + dx_{i+1}} \frac{f_i - f_{i-1}}{dx_i}$$

$$\left(\frac{\partial^2 f}{\partial x^2}\right)_i = 2\left(\frac{f_{i+1}}{(dx_i + dx_{i+1})dx_{i+1}} + \frac{f_{i-1}}{(dx_i + dx_{i+1})dx_i} - \frac{f_i}{dx_i dx_{i+1}}\right) . \tag{19}$$

The resulting finite-difference equation takes the form:

$$Ac_{ij}\phi_{ij} + Ae_{ij}\phi_{i+1,j} + Aw_{ij}\phi_{i-1,j} + An_{ij}\phi_{i,j+1} + As_{i,j}\phi_{i,j-1} + Aen_{ij}\phi_{i+1,j+1} + Aes_{ij}\phi_{i+1,j-1}$$

$$+Awn_{ij}\phi_{i-1,j+1} + Aws_{ij}\phi_{i-1,j-1} = R_{ij} \tag{20}$$

where R_{ij} is the residual of equation (11) at node (i,j) and ϕ^{ij} is the difference in the variable T evaluated at the current and previous steps. This leads to

$$A\ \phi = R. \tag{21}$$

The finite-difference matrix A is a nine-diagonal coefficient matrix. It is approximated by incomplete factorization i.e. $A=L^*U^*$, where L^* is a lower triangular matrix and U^* is an upper Triangular matrix, and the factors are easy to calculate. The approximate factors L and U may have the sparsity structure of the original matrix. The solution for equation (21) is straightforward since it consists of forward substitution

$$U^*\ \phi = (L^*)^{-1}\ R, \tag{22}$$

followed by a backward substitution,

$$\phi = (U^*)^{-1}\ (L^*)^{-1}R. \tag{23}$$

The subsequent approximations are obtained via

$$T^{m+1} = T^m + \lambda\ \phi\ , \tag{24}$$

where λ is a relaxation parameter. Unfortunately, such an iteration scheme generally converges slowly, so an acceleration technique must be added. Alternative acceleration techniques which have been developed are conjugate direction methods. For sparse symmetric positive-definite linear systems the preconditioned conjugate residual method is one of the best. However, equation (11) is far from symmetric, therefore, in the present investigation the preconditioned generalized conjugate residual (PGCR) method is the chosen acceleration technique since it was developed specifically for nonsymmetric systems.

The PGCR procedure is as follows:

Initialize

$$T^0$$

$$R^0 = F - LT^0$$

$$A\phi^0 = R^0$$

$$P^0 = \phi^0$$

Iterate

$$\alpha_{m+1} = \frac{(R^m, LP^m)}{(LP^m, LP^m)}$$

$$T^{m+1} = T^m + \alpha_{m+1} P^m$$

$$R^{m+1} = R^m - \alpha_{m+1} LP^m \qquad (25)$$

$$A\phi^{m+1} = R^{m+1}$$

$$\beta_j^{m+1} = -\frac{\left(L\phi^{m+1}, LP^j\right)}{\left(LP^j, LP^j\right)}$$

$$P^{m+1} = \phi^{m+1} + \sum_{j=0}^{m} \beta_j^{m+1} P^j$$

The scalar α is chosen to minimize the Euclidean norm of the residual. The β's are orthogonality coefficients and result from the orthogonality property for the conjugate residual version. The practical calculation only requires the following condition to terminate the iteration

$$\max \frac{\left|T^{m+1} - T^m\right|}{T^{m+1}} \leq \varepsilon , \qquad (26)$$

where we took $\varepsilon = 10^{-7}$.

The PGCR method is an attractive iterative method for solving non-symmetric system since the iteration cannot break down, it is stable and the minimization increases the convergence rate considerably. We compared the PGCR method to a Conjugate Gradient Squared (CGS) method and a Strongly Implicit Procedure (SIP). For all these methods, we also used incomplete factorization to solve the preconditioned problem. The results show that PGCR method is more efficient in terms of CPU time.

Outer iteration

Having computed the new values of temperature, an outer-loop iteration is required to update the melt/solid interface h(r) at which the computed temperature is equal to Tmelt. One scheme to update the interface shape is Newton's method

$$h_i^{L+1} = h_i^L - \left(\frac{\partial F}{\partial h}\right)_i^{-1} F_i , \qquad (27)$$

where $F_i = T_{i,j}^* - T_{melt}$, here $T_{i,j}^*$ is the calculated temperature at the Lth interface location. However for Newton's method, it is difficult to guarantee the outer iteration convergence for all cases. Therefore as an alternative to Newton's method, an interpolation scheme is used to update the interface. In the present study, the new interface is located by the following linear interpolation:

$$\text{if } T_m \leq T_{ij} \text{ and } T_m > T_{i,j+1}$$

$$h_i^{L+1} = z_j + \frac{(T_{ij} - T_m)}{(T_{ij} - T_{i,j+1})} * (z_{j+1} - z_j) . \tag{28}$$

The outer-loop iteration is continued until the following convergence criterion is satisfied:

$$ER = \max \left| \frac{h^{L+1} - h^{L}}{h^{L+1}} \right| \leq \varepsilon , \tag{29}$$

where we took $\varepsilon = 10^{-4}$.

Results and discussion

For the purposes of comparison of our method with that of Adornato and Brown [2] (for cases in which convection did not influence the interface shape) we have carried out numerical simulations for the growth (in the absence of convection) of a gallium-doped germanium (Ga:Ge) alloy in a vertical Bridgman system. (Thus, our computed interface shapes, which are for solidification in the absence of convection could be compared with theirs). The calculations for Ga:Ge growth are presented separately for the two furnaces and the different ampoule. For a heat-pipe furnace, the changes in the heat transfer coefficient between ampoule and three zones of furnace are modelled by the function

$$Bi(z) = \frac{Bi_0}{2}(c_3\{1 + \tanh[c_1(z_c - c_2 - z)]\} + 1 + \tanh[-c_1(z_c + c_2 - z)]) ,$$

where z_c is the location of the mid-plane of gradient zone. The Bi_0 is the value of Biot number in the cold zone, c_3 sets the ratio between the Biot numbers in the hot and cold zone, c_1 is the slope of the transition in Bi (z) between the isothermal zones and the adiabatic region, and c_2 is the half of the dimensionless length of the adiabatic zone. The furnace wall temperature is modelled by the function

$$T_f(z) = 0.5\{1 + \tanh[12(0.5 - z/\Lambda)]\},$$

where the constants in this expression have been fit to the measured wall temperature of the furnace. For details of the thermophysical properties and growth conditions the reader is referred to [2].

For a heat pipe furnace and a boron nitride ampoule, the temperature field is shown in Fig.12a. The difference between the thermal conductivities of the melt, crystal and ampoule cause the melt /crystal interface to be convex with respect to the melt and results in the temperature decreasing radially adjacent to the phase boundary. The mismatch in thermal boundary conditions between the adiabatic and hot zones of the furnace causes a second set of radial gradients with the hottest temperature located at the ampoule wall. Fig.12b depicts the temperature field using a quartz ampoule (in a heat pipe furnace) which decreases the conductivity of the ampoule to a factor of 14 lower than the melt. As seen by Adornato and Brown, the ampoule wall takes up most of the radial temperature difference required to transport heat in the system. Thus, the interface is flatter, and the radial temperature gradients near the interface are smaller. Larger radial temperature gradients occur near the intersection of the adiabatic and hot (cold) zones.

The constant gradient furnace is modelled by using a constant Biot number over the entire length of the ampoule and specifying the furnace temperature profile as

$$T_f = 1 - z/\Lambda .$$

The isotherms are almost flat, the large radial gradients that arise at the intersection of adiabatic and hot (cold) regions in the heat-pipe furbace is eleminated, and the deflection of the melt/crystal interface is large as indicated seen in Fig. 2.c.

In addition to the work described above, we have started to add convection in the melt phase. The biggest problem encountered to date appears to be that of convergence rates which at present are excessively slow even with the finite difference preconditioning.

Future Work

Work planned for the next six monthly period includes the incorporation of melt convection into the model. Based on our experience with convergence rates for the problem of convection in a cylinder (see section **4.3**) using the influence matrix method (without preconditioning) the prospects of obtaining an efficient solution method for the coupled convection-solidification problem are presently not good. We will thus continue to investigate convergence acceleration techniques for spectral methods.

References

[1] J. Ouazzani, *Méthode Pseudo-spectrale pour la Resolution des Equations d'un Melange de Gaz Binaire*, Thèse, Universitie de Nice (1984).

[2] P.M. Adornato and R.A. Brown, J. Crystal Growth 80 (1987) 155.

4.3 The Influence Matrix Method Applied to Convection in a Cylinder

Governing equations

For an axisymmetric system, in cylindrical coordinates the heat and momentum transport equations in stream function - vorticity form may be written as

$$\frac{\partial\tilde{T}}{\partial\tilde{t}} + \tilde{u}\cdot\tilde{\nabla}\tilde{T} = \alpha\tilde{\nabla}^2\tilde{T}, \tag{1}$$

$$\frac{\partial\tilde{\omega}_\theta}{\partial\tilde{t}} + \tilde{u}_r\frac{\partial\tilde{\omega}_\theta}{\partial\tilde{r}} + \tilde{u}_z\frac{\partial\tilde{\omega}_\theta}{\partial z} - \frac{\tilde{\omega}_\theta\tilde{u}_r}{\tilde{r}} = \nu\left(\frac{\partial^2\tilde{\omega}_\theta}{\partial\tilde{r}^2} + \frac{1}{\tilde{r}}\frac{\partial\tilde{\omega}_\theta}{\partial\tilde{r}} + \frac{\partial^2\tilde{\omega}_\theta}{\partial\tilde{r}^2} - \frac{\tilde{\omega}_\theta}{\tilde{r}^2}\right) + \beta g_z\frac{\partial\tilde{T}}{\partial\tilde{r}}, \tag{2}$$

$$\frac{\partial^2\tilde{\psi}}{\partial\tilde{r}^2} - \frac{1}{\tilde{r}}\frac{\partial\tilde{\psi}}{\partial\tilde{r}} + \frac{\partial^2\tilde{\psi}}{\partial\tilde{z}^2} = \tilde{r}\tilde{\omega}_\theta, \tag{3}$$

where $\tilde{T}$ represents temperature, $\tilde{\omega}_\theta$ the azimuthal component of the vorticity, $\tilde{\psi}$ the stream function, $\tilde{t}$ time, α the thermal diffusivity, ν the kinematic viscosity, β the coefficient of thermal expansion, g_z the axial component of the gravitational acceleration, $\tilde{u}$ the velocity vector, and $\tilde{u}_z, \tilde{u}_r$ the axial and radial components of the velocity, respectively. The " ˜ " indicates a dimensional variable.

The stream function $\tilde{\psi}$ in eqn. (3) is defined by

$$\tilde{u}_r = \frac{1}{\tilde{r}}\frac{\partial\tilde{\psi}}{\partial\tilde{z}}, \quad \tilde{u}_z = -\frac{1}{\tilde{r}}\frac{\partial\tilde{\psi}}{\partial\tilde{z}}, \tag{4}$$

and the azimuthal component of vorticity is defined by

$$\tilde{\omega}_\theta = \frac{\partial\tilde{u}_r}{\partial\tilde{z}} - \frac{\partial\tilde{u}_z}{\partial\tilde{r}} \tag{5}$$

For an axisymmetric system the two other components of vorticity are identically zero.

Due to the extra diffusive component in eqn. (2) $\tilde{\omega}_\theta/\tilde{r}^2$, which arises in cylindrical coordinates, an alternative variable $\tilde{S} \equiv \tilde{r}\tilde{\omega}_\theta$ must be solved for so that the discretization in time is consistent (details given below). Therefore

$$\frac{\partial\tilde{S}}{\partial\tilde{t}} + \tilde{u}_r\frac{\partial\tilde{S}}{\partial\tilde{r}} + \tilde{u}_z\frac{\partial\tilde{S}}{\partial\tilde{z}} - \frac{2\tilde{S}\tilde{u}_r}{\tilde{r}} = \nu\left(\frac{\partial^2\tilde{S}}{\partial\tilde{r}^2} - \frac{1}{\tilde{r}}\frac{\partial\tilde{S}}{\partial\tilde{r}} + \frac{\partial^2\tilde{S}}{\partial\tilde{z}^2}\right) + \tilde{r}\beta g_z\frac{\partial\tilde{T}}{\partial\tilde{r}}, \tag{6}$$

and

$$\frac{\partial^2\tilde{\psi}}{\partial\tilde{r}^2} - \frac{1}{\tilde{r}}\frac{\partial\tilde{\psi}}{\partial\tilde{r}} + \frac{\partial^2\tilde{\psi}}{\partial\tilde{z}^2} = \tilde{S}, \tag{7}$$

are solved for in place of eqn.s (2) and (3).

Equations (1), (6), and (7) are solved inside a cylinder of radius R and height H. Due to axisymmetry, the boundary condition

$$\left.\frac{\partial\tilde{T}}{\partial\tilde{r}}\right|_{\tilde{r}=0} = 0, \tag{8}$$

is applied at the centerline. Dirichlet, Neumann, or Cauchy boundary conditions may be applied for the temperature at the top, bottom, and side of the cylinder.

The no-slip condition for the fluid velocity at the top, bottom, and side of the cylinder results in the boundary conditions

$$\left.\frac{\partial\tilde{\psi}}{\partial\tilde{z}}\right|_{\tilde{z}=\frac{H}{2}} = 0, \quad \left.\frac{\partial\tilde{\psi}}{\partial\tilde{z}}\right|_{\tilde{z}=-\frac{H}{2}} = 0, \quad \left.\frac{\partial\tilde{\psi}}{\partial\tilde{r}}\right|_{\tilde{r}=0} = 0, \tag{9}$$

for the stream function. Since the value of the stream function is arbitrary to within a constant, its value is set to zero at the top, bottom, and side of the cylinder. This combined with the condition of no penetration for the fluid velocity at the centerline determines the value of the stream function at the centerline to be zero.

Because of axisymmetry, S=0 at the centerline. As is the case for vorticity in the stream function - vorticity formulation, the boundary conditions for S at the other three boundaries are not predeterminable.

The general approach of scaling the velocities by a characteristic velocity U, the times by a characteristic time t, and lengths by a characteristic length L results in the nondimensional equations

$$(\mathrm{Fo})^{-1}\frac{\partial\Theta}{\partial t} + \mathrm{Pr}\,\mathrm{Re}\left(u_r\frac{\partial\Theta}{\partial r} + u_z\frac{\partial\Theta}{\partial z}\right) = \frac{\partial^2\Theta}{\partial r^2} + \frac{1}{r}\frac{\partial\Theta}{\partial r} + \frac{\partial^2\Theta}{\partial z^2}, \tag{10}$$

$$(\mathrm{Fo}\,\mathrm{Pr})^{-1}\frac{\partial S}{\partial t} + \mathrm{Re}\left(u_r\frac{\partial S}{\partial r} + u_z\frac{\partial S}{\partial z} - \frac{2Su_r}{r}\right) = \frac{\partial^2 S}{\partial r^2} - \frac{1}{r}\frac{\partial S}{\partial r} + \frac{\partial^2 S}{\partial z^2} - r\frac{\mathrm{Ra}}{\mathrm{Re}\,\mathrm{Pr}}\frac{\partial\Theta}{\partial r}, \tag{11}$$

$$\frac{\partial^2\psi}{\partial r^2} - \frac{1}{r}\frac{\partial\psi}{\partial r} + \frac{\partial^2\psi}{\partial z^2} = S, \tag{12}$$

where Fo, Pr, Re, and Ra are the Fourier Number, the Prandtl Number, the Reynolds Number, and the Rayleigh Number. The definitions of these four nondimensional quantities are given in a table at the end of this section. The three field variables are defined by

$$\Theta \equiv \frac{\tilde{T} - T_{ref}}{\Delta T}, \quad S \equiv \frac{\tilde{S}}{U}, \quad \psi \equiv \frac{\tilde{\psi}}{UL^2}, \tag{13}$$

where ΔT is a characteristic temperature difference and T_{ref} is a reference temperature.

In nondimensionalizing the boundary conditions it is convenient to choose the characteristic length to be half the radius (i.e. $L = R/2$). With this choice the boundary conditions for equation (10) are

$$\left.\frac{\partial \Theta}{\partial r}\right|_{r=0} = 0, \tag{14}$$

and at the top ($z = +1/L$), bottom ($z = -1/L$), and side of the cylinder ($r = 2$) Dirichlet, Neumann, or Cauchy conditions may be applied. Note that $\Lambda = R/H$ is the aspect ratio. For equation (11) the boundary condition at the centerline is $S=0$, and the boundary conditions at the top, bottom, and side of the cylinder are not predeterminable. The boundary conditions for equation (12) are

$$\left.\frac{\partial \psi}{\partial r}\right|_{r=2} = 0, \quad \left.\frac{\partial \psi}{\partial z}\right|_{z=+1/\Lambda} = 0, \quad \left.\frac{\partial \psi}{\partial z}\right|_{z=-1/\Lambda} = 0, \tag{15}$$

and

$$\psi = 0 \text{ at } r = 0, \quad \psi = 0 \text{ at } r = 2, \quad \psi = 0 \text{ at } z = 1/\Lambda, \quad \psi = 0 \text{ at } z = -1/\Lambda, \tag{16}$$

Numerical Method

Equations (10), (11), and (12) are discretized in time using a semi-implicit scheme for the diffusive terms and an explicit scheme for the convective terms. Rearranging the discretized equations into the form necessary for their solution by means of a Helmholtz solver yields

$$\begin{aligned} &\left(\frac{\partial^2 \Theta}{\partial r^2} + \frac{1}{r}\frac{\partial \Theta}{\partial r} + \frac{\partial^2 \Theta}{\partial z^2}\right)^{n+1} - \frac{3}{2\,\Delta t\,\mathrm{Fo}}\,\Theta^{n+1} \\ &= \frac{\Theta^{n-1} - 4\Theta^{n}}{2\,\Delta t\,\mathrm{Fo}} + \Pr \mathrm{Re}\left[2\left(u_r\frac{\partial \Theta}{\partial r} + u_z\frac{\partial \Theta}{\partial z}\right)^{n} - \left(u_r\frac{\partial \Theta}{\partial r} + u_z\frac{\partial \Theta}{\partial z}\right)^{n-1}\right] \end{aligned} \tag{17}$$

$$\left(\frac{\partial^2 S}{\partial r^2} - \frac{1}{r}\frac{\partial S}{\partial r} + \frac{\partial^2 S}{\partial z^2}\right)^{n+1} - \frac{3}{2\,\Delta t\,\mathrm{Fo}\,\mathrm{Pr}}\,S^{n+1}$$

$$= \frac{S^{n-1} - 4S^{n}}{2\,\Delta t\,\mathrm{Fo}\,\mathrm{Pr}} + \mathrm{Re}\left[2\left(u_r\frac{\partial S}{\partial r} + u_z\frac{\partial S}{\partial z} - \frac{2\,S\,u_r}{r}\right)^{n} - \left(u_r\frac{\partial S}{\partial r} + u_z\frac{\partial S}{\partial z} - \frac{2\,S\,u_r}{r}\right)^{n-1}\right] + \frac{r\,\mathrm{Ra}}{\mathrm{Re}\,\mathrm{Pr}}\frac{\partial \Theta}{\partial r}^{n+1} \tag{18}$$

$$\frac{\partial^2 \psi^{n+1}}{\partial r^2} - \frac{1}{r}\frac{\partial \psi^{n+1}}{\partial r} + \frac{\partial^2 \psi^{n+1}}{\partial z^2} = S^{n+1}, \tag{19}$$

where the integers n-1, n, n+1 indicate the number of the time step.

Due to the lack of boundary conditions for equation (18), the method of the matrix of influence is used for the solution of the momentum part of the problem, that is equations (18) and (19). In the method of the matrix of influence first a preprocessing stage must be completed. In this stage a set of elementary solutions are calculated. These elementary solutions are defined by

$$\frac{\partial^2 S_j}{\partial r^2} - \frac{1}{r}\frac{\partial S_j}{\partial r} + \frac{\partial^2 S_j}{\partial z^2} - \frac{3}{2\,\Delta t\,\mathrm{Fo}\,\mathrm{Pr}}\,S_j = 0, \tag{20}$$

with boundary conditions

$$\begin{gathered} S_j(\eta_i) = \delta_{ij}, \quad \eta_i \in \Gamma_{MI}, \\ S_j(\eta_i) = 0, \quad \eta_i \in \Gamma - \Gamma_{MI}, \\ S_j(\eta_i) = 0, \quad r = 0, \end{gathered} \tag{21}$$

and

$$\frac{\partial^2 \psi_j}{\partial r^2} - \frac{1}{r}\frac{\partial \psi_j}{\partial r} + \frac{\partial^2 \psi_j}{\partial z^2} = S_j, \tag{22}$$

with boundary conditions

$$\psi_j = 0, \ \text{at}\ r = 0, r = 2, z = \frac{1}{\Lambda}, z = \frac{-1}{\Lambda}, \tag{23}$$

where δ_{ij} is the Kronecker delta, η_i are the collocation points that lie on the boundary of the computational domain, Γ represents all of the boundary except for the centerline, and Γ_{MI} is the special matrix of influence subset of Γ. The final two steps of the preprocessing stage are the generation of the matrix of influence, and then to take its inverse. The matrix of influence is

$$M_{ij} = \frac{\partial \psi_j(\eta_i)}{\partial \hat{n}}, \quad \eta_i \in \Gamma_{MI}, \tag{24}$$

where $\hat{n}$ is the outward pointing unit normal at each boundary. Due to the occurence of Δt in equation (20) the preprocessing steps must be repeated if the size of the time step is changed.

At each time step seven stages are completed. The first stage is solution of

$$\frac{\partial^2 \hat{S}}{\partial r^2} - \frac{1}{r}\frac{\partial \hat{S}}{\partial r} + \frac{\partial^2 \hat{S}}{\partial z^2} - \frac{3}{2\,\Delta t\,\mathrm{Fo}\,\mathrm{Pr}}\hat{S}$$
$$= \frac{S^{n-1} - 4S^n}{2\,\Delta t\,\mathrm{Fo}\,\mathrm{Pr}} + \mathrm{Re}\left[2\left(u_r\frac{\partial S}{\partial r} + u_z\frac{\partial S}{\partial z} - \frac{2\,S\,u_r}{r}\right)^n - \left(u_r\frac{\partial S}{\partial r} + u_z\frac{\partial S}{\partial z} - \frac{2\,S\,u_r}{r}\right)^{n-1}\right] + \frac{r\,\mathrm{Ra}}{\mathrm{Re}\,\mathrm{Pr}}\frac{\partial \Theta^{n+1}}{\partial r}, \tag{25}$$

with boundary conditions

$$\hat{S} = 0, \ \text{at } r = 0, r = 2, z = \frac{1}{\Lambda}, z = \frac{-1}{\Lambda}. \tag{26}$$

The second stage is solution of

$$\frac{\partial^2 \hat{\psi}}{\partial r^2} - \frac{1}{r}\frac{\partial \hat{\psi}}{\partial r} + \frac{\partial^2 \hat{\psi}}{\partial z^2} = \hat{S}, \tag{27}$$

with boundary conditions

$$\hat{\psi} = 0, \ \text{at } r = 0, r = 2, z = \frac{1}{\Lambda}, z = \frac{-1}{\Lambda}. \tag{28}$$

Using $\hat{\psi}$ from the second stage, in the third stage $\bar{h}$ is generated:

$$\bar{h}(\eta_i) = -\frac{\partial \hat{\psi}(\eta_i)}{\partial \hat{n}}, \quad \eta_i \in \Gamma_{MI}. \tag{29}$$

In the fourth stage λ_i is generated:

$$\lambda_i = \lambda(\eta_i) = M^{-1}{}_{ij}\,\bar{h}(\eta_j). \tag{30}$$

The fifth stage is the solution of equation (18) with boundary conditions

$$\begin{gathered} S^{n+1}(\eta_i) = \lambda_i, \quad \eta_i \in \Gamma_{MI}, \\ S^{n+1}(\eta_i) = 0, \ \eta_i \in \Gamma - \Gamma_{MI}, \\ S^{n+1}(\eta_i) = 0, \ r = 0, \end{gathered} \tag{31}$$

In the sixth stage the stream function at the $(n+1)^{th}$ time step is generated by solving equation (19) with boundary conditions

$$\psi^{n+1} = 0 \text{ at } r = 0, \ \psi^{n+1} = 0 \text{ at } r = 2, \ \psi^{n+1} = 0 \text{ at } z = 1/\Lambda, \ \psi^{n+1} = 0 \text{ at } z = -1/\Lambda. \tag{32}$$

Finally, in the seventh stage the true values of S^{n+1} on the boundary are calculated by evaluating the left-hand side of equation (19).

Non-Dimensional Groups

Fourier Number	$Fo \equiv \alpha\, \tau / L^2$
Prandtl Number	$Pr \equiv \nu / \alpha$
Reynolds Number	$Re \equiv U\, L / \nu$
Rayleigh Number	$Ra \equiv \beta\, g\, \Delta T\, L^3 / \nu\, \alpha$

5. Presentations and Publications

From the work carried out under this grant the following papers have been published, accepted for publication or are in preparation for submission for publication:

1. A. Nadarajah, F. Rosenberger and J. I. D. Alexander, *Modelling the Solution Growth of Triglycine Sulfate in Low Gravity,* J. Crystal Growth **104** (1990) 218-232.
2. F. Rosenberger, J. I. D. Alexander, A. Nadarajah and J. Ouazzani, Influence of Residual Gravity on Crystal Growth Processes, Microgravity Sci. Technol. **3** (1990) 162-164.
3. J. P. Pulicani and J. Ouazzani, *A Fourier-Chebyshev Pseudo-Spectral Method for Solving Steady 3-D Navier-Stokes and Heat Equations in Cylindrical Cavities*, Computers and Fluids **20** (1991) 93.
4. J. P. Pulicani, S. Krukowski, J. I. D. Alexander, J. Ouazzani and F. Rosenberger, *Convection in an Asymmetrically Heated Cylinder*, Int. J. Heat Mass Transfer (accepted)
5. F. Rosenberger, J. I. D. Alexander and W.-Q. Jin, *Gravimetric Capillary Method for Kinematic Viscosity Measurements,* Rev. Sci. Instr. (submitted).
6. A. Nadarajah, F. Rosenberger and T. Nyce, *Interferometric Technique for Diffusivity Measurements in (Supersaturated) Solutions,* in preparation.

In addition to the above publications, the results of our work have been presented at the following conferences:

1. "Commercial Numerical Codes: To Use or Not to Use, Is This The Question?" presented by J.I.D Alexander at the Microgravity Fluids Workshop, Westlake Holiday Inn, Cleveland Ohio, August 7-9, 1990.
2. "Fluid Transport in Materials Processing" presented by F. Rosenberger at the Microgravity Fluids Workshop, Westlake Holiday Inn, Cleveland Ohio, August 7-9, 1990.

3. "Influence of Residual Gravity on Crystal Growth Processes," presented by F. Rosenberger at the First International Microgravity Congress, Bremen, September (1990).
4. "Modelling the Solution Growth of TGS Crystals in Low Gravity", presented by A. Nadarajah at the Eighth American Conference on Crystal Growth (July 15-21, 1990, Vail, Colorado).
5. "Modelling the Solution Growth of TGS Crystals in Low Gravity", presented by J. I. D. Alexander at the Committee on Space Research (COSPAR) Plenary Meeting (June 26 - July 6, 1990, The Hague, Netherlands).
6. "An Analysis of the Low Gravity Sensitivity of the Bridgman-Stockbarger Technique", presented by J. I. D. Alexander to the Department of Mechanical Engineering at Clarkson University, April, 1991.
7. "Residual Acceleration Effects on Low Gravity Experiments". A 3-lecture series presented by J. I. D. Alexander at the Institute de Mechaniques des Fluides de Marseilles, Université de Aix-Marseille III, Marseille, France, January, 1991.
8. "Measuring Diffusion Coefficients of Concentrated Solutions, presented by A. Nadarajah at the Fifth Annual Alabama Materials Research Conference, Birmingham September 1991.
9. "Modelling Crystal Growth Under Low Gravity", presented by A. Nadarajah at the Annual Technical Meeting of the Society of Engineering Science, Gainesville, November 1991.

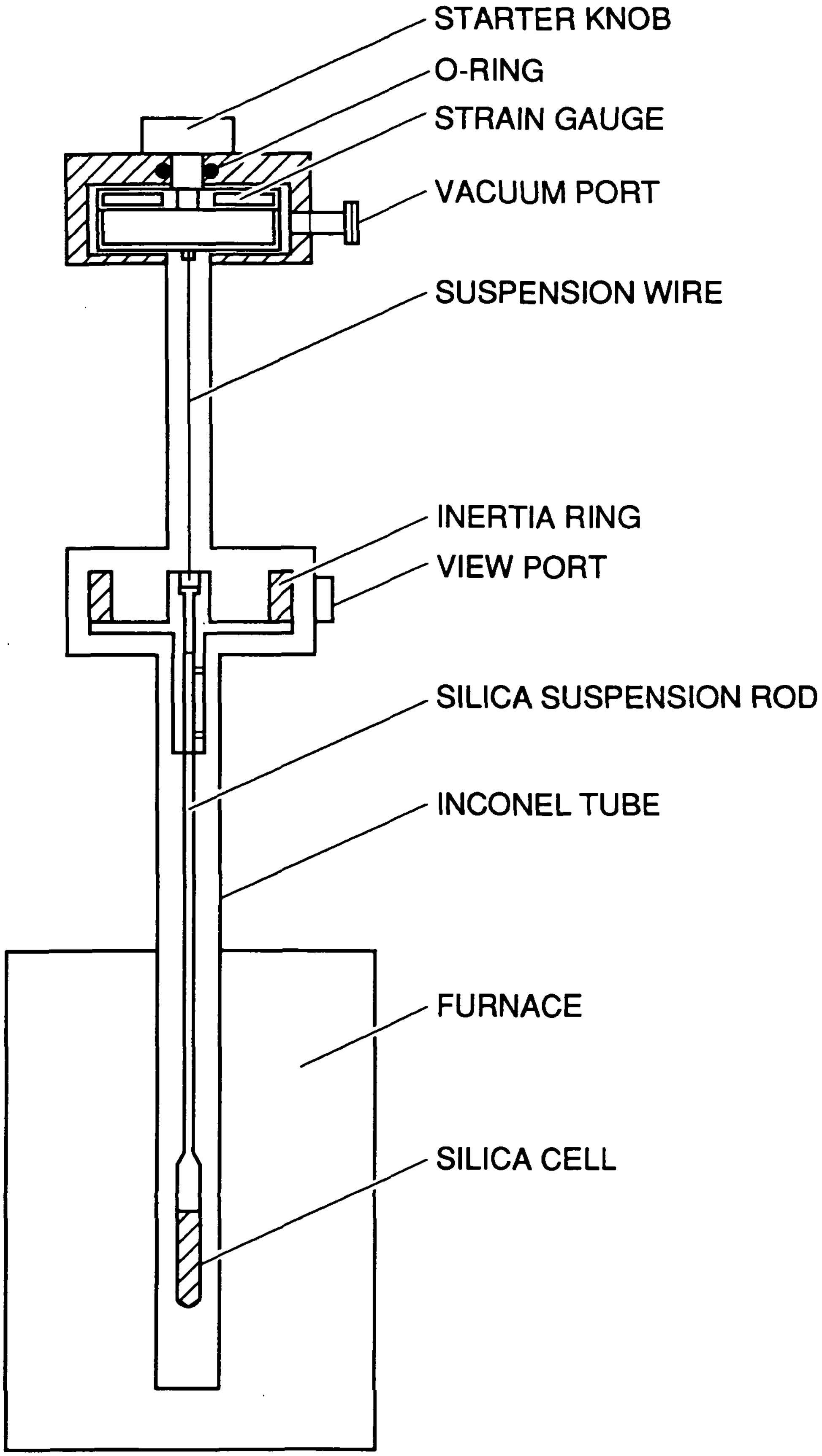
STARTER KNOB
O-RING
STRAIN GAUGE
VACUUM PORT
SUSPENSION WIRE
INERTIA RING
VIEW PORT
SILICA SUSPENSION ROD
INCONEL TUBE
FURNACE
SILICA CELL

FIG. 1

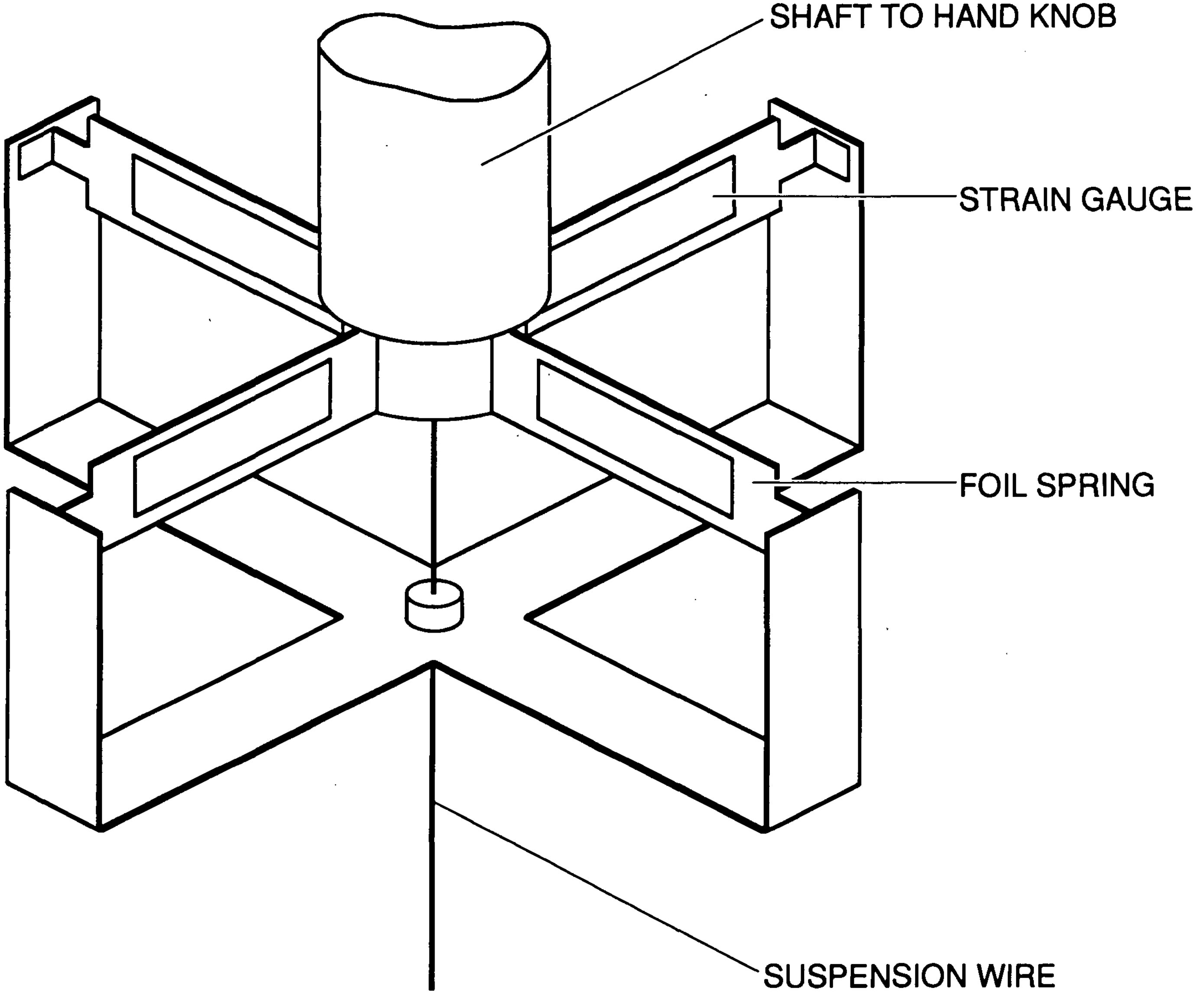
SHAFT TO HAND KNOB
STRAIN GAUGE
FOIL SPRING
SUSPENSION WIRE

FIG. 2

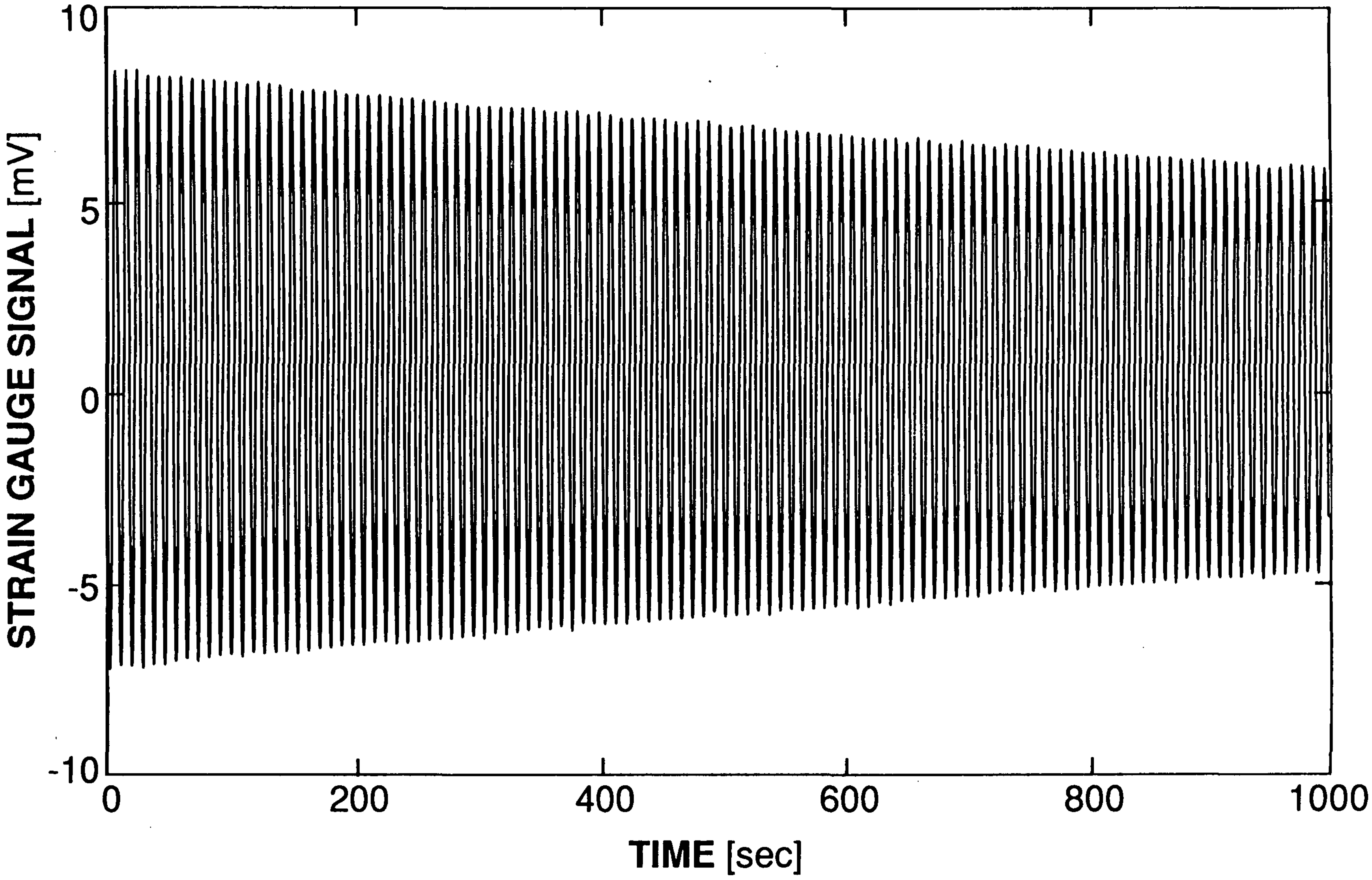

10
5
0
-5
-10
0
200
400
600
800
1000
STRAIN GAUGE SIGNAL [mV]
TIME [sec]

FIG. 3

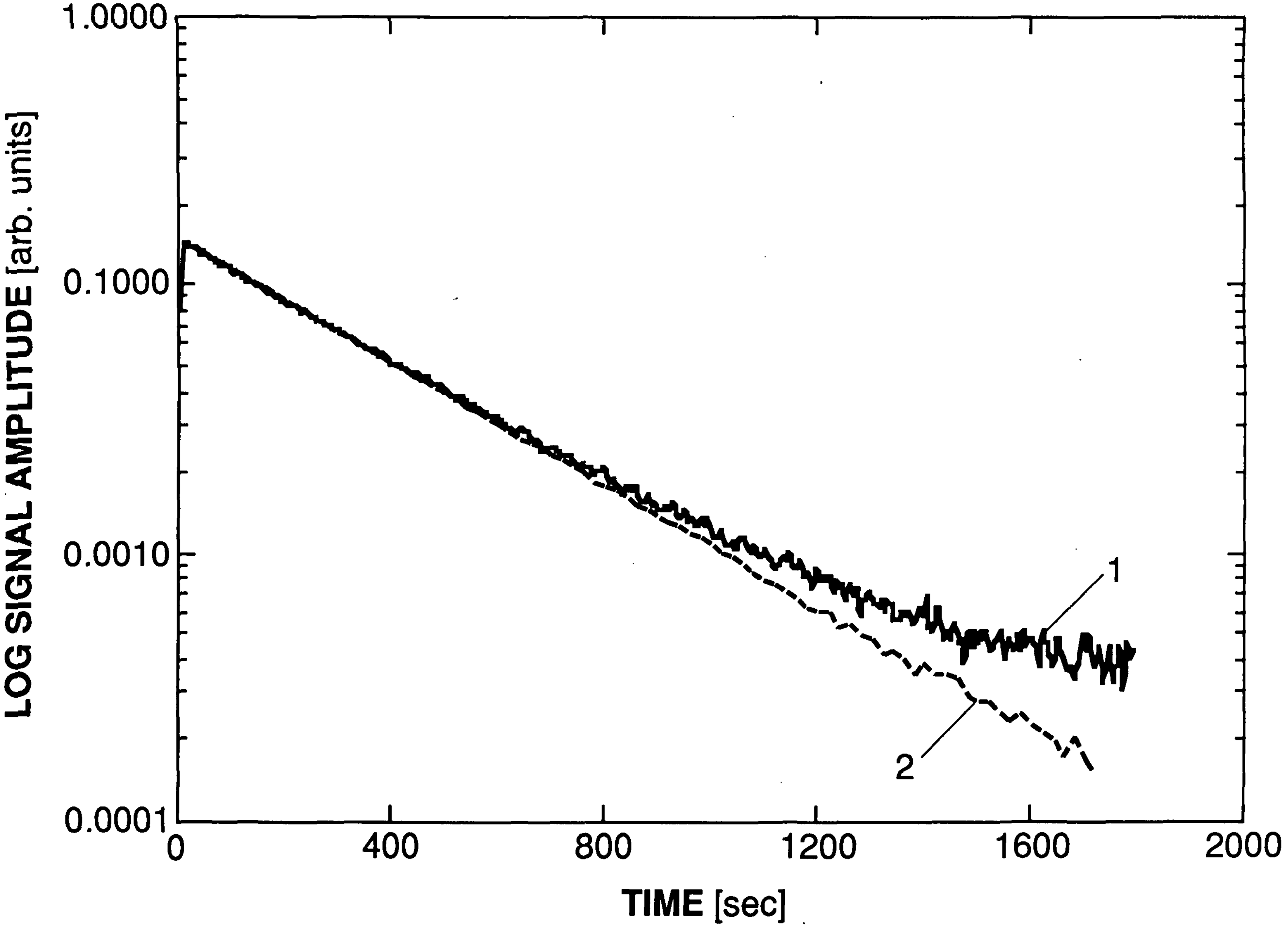
1.0000
0.1000
0.0010
0.0001
LOG SIGNAL AMPLITUDE [arb. units]
0
400
800
1200
1600
2000
TIME [sec]
1
2

FIG. 4

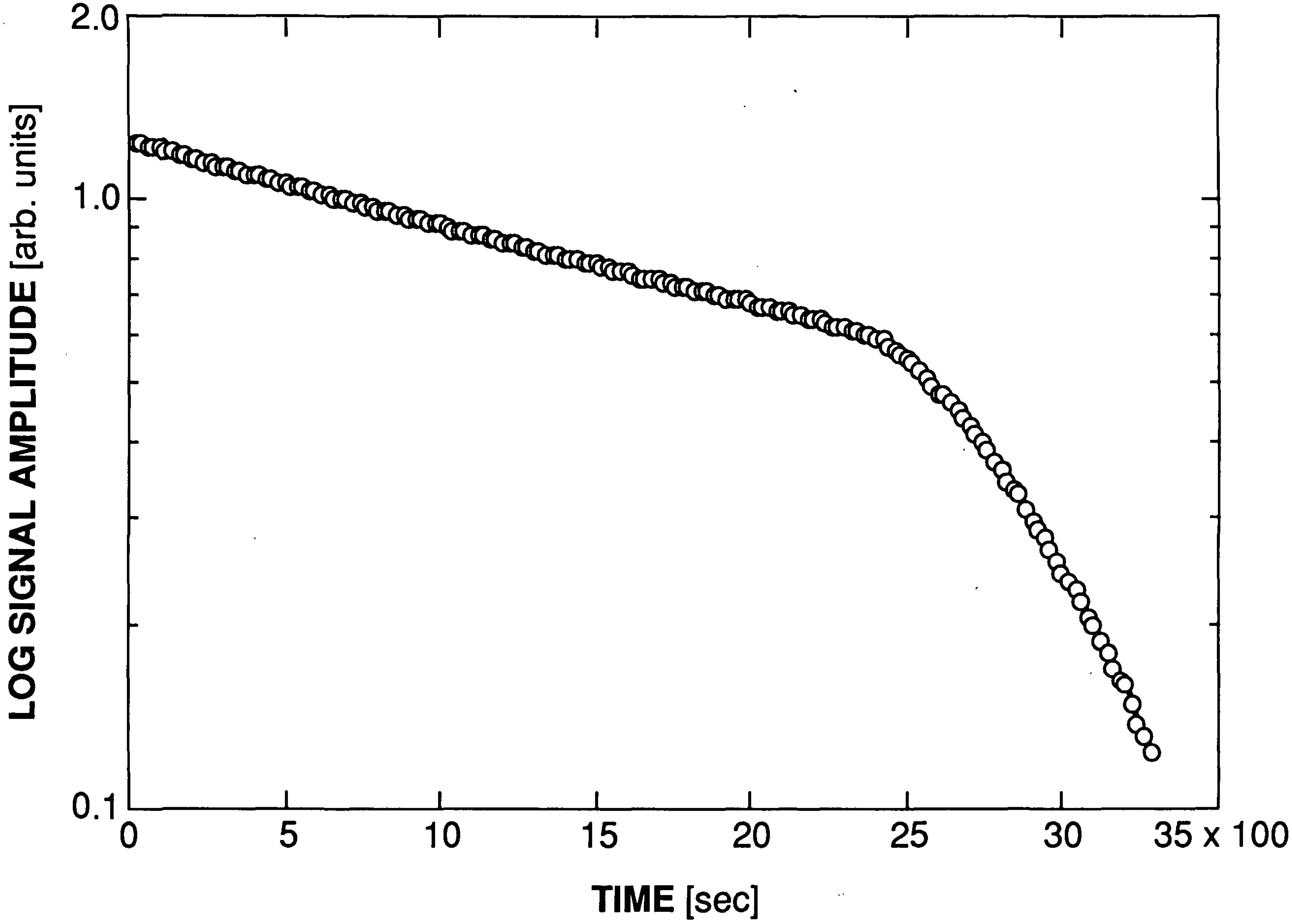
2.0
1.0
0.1
LOG SIGNAL AMPLITUDE [arb. units]
0
5
10
15
20
25
30
35 x 100
TIME [sec]

FIG. 5

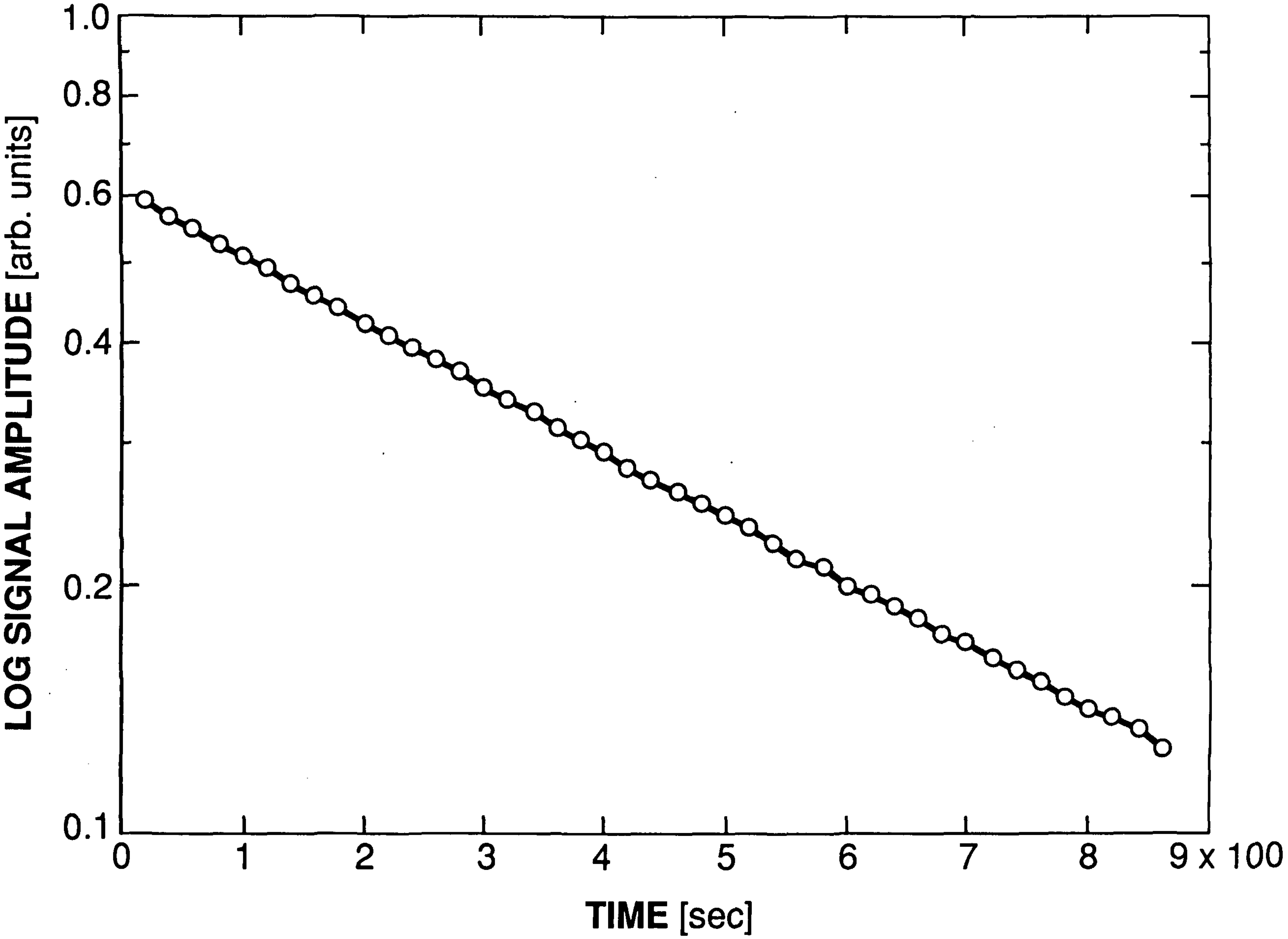
LOG SIGNAL AMPLITUDE [arb. units]
1.0
0.8
0.6
0.4
0.2
0.1
0
1
2
3
4
5
6
7
8
9 x 100
TIME [sec]

FIG. 6

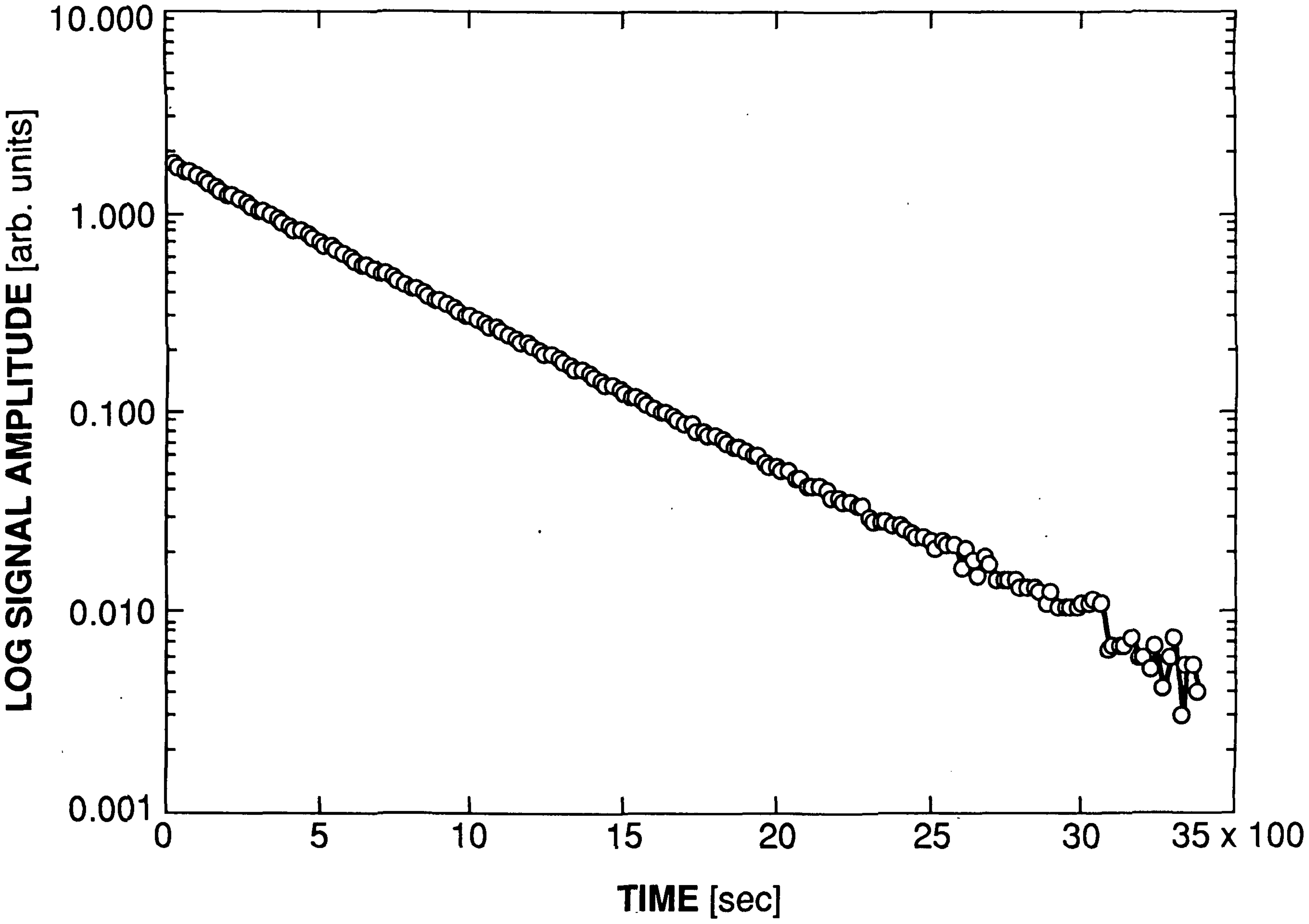
LOG SIGNAL AMPLITUDE [arb. units]
10.000
1.000
0.100
0.010
0.001
0
5
10
15
20
25
30
35 x 100
TIME [sec]

FIG. 7

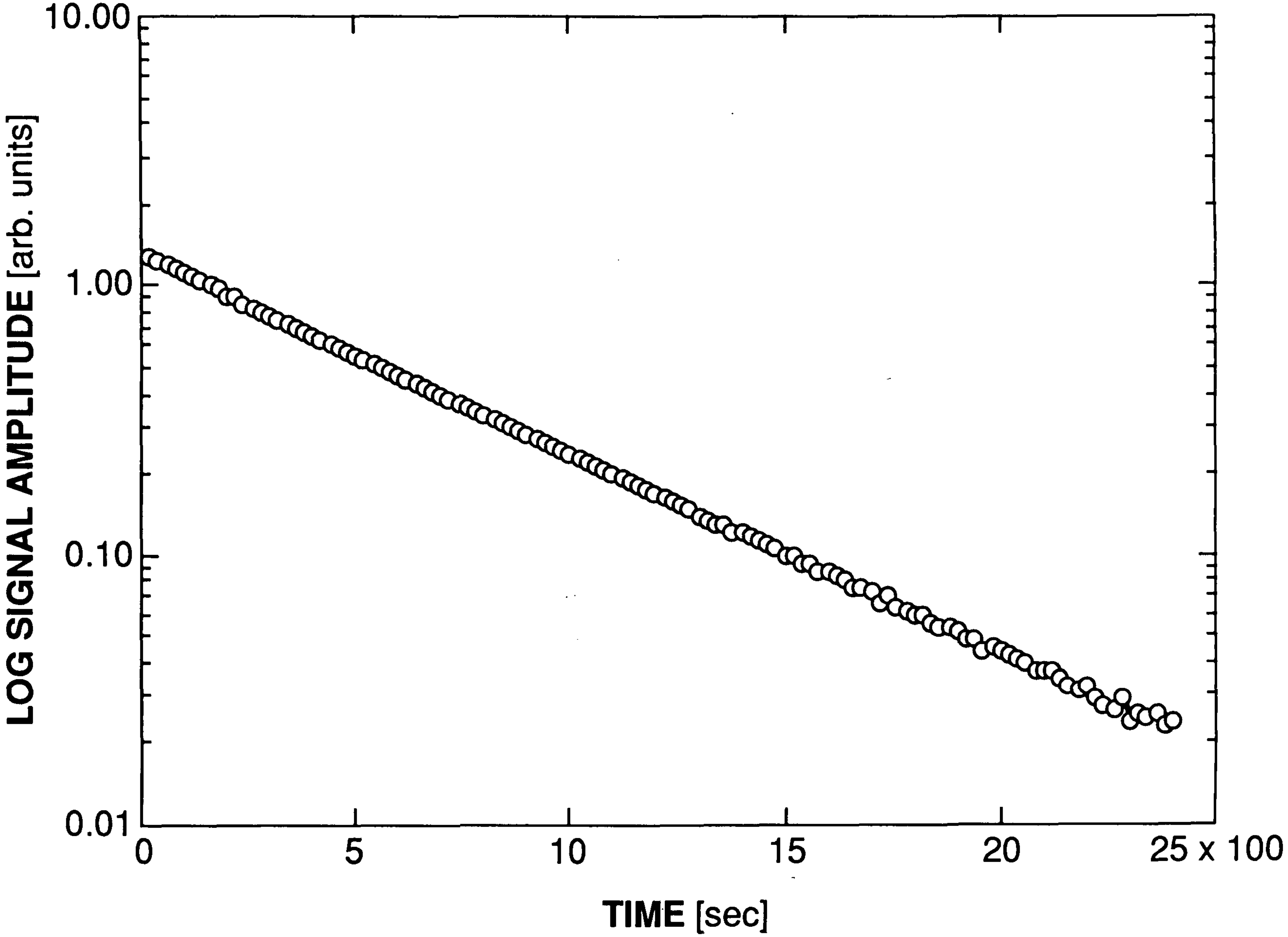
10.00
1.00
0.10
0.01
LOG SIGNAL AMPLITUDE [arb. units]
0
5
10
15
20
25 x 100
TIME [sec]

FIG. 8

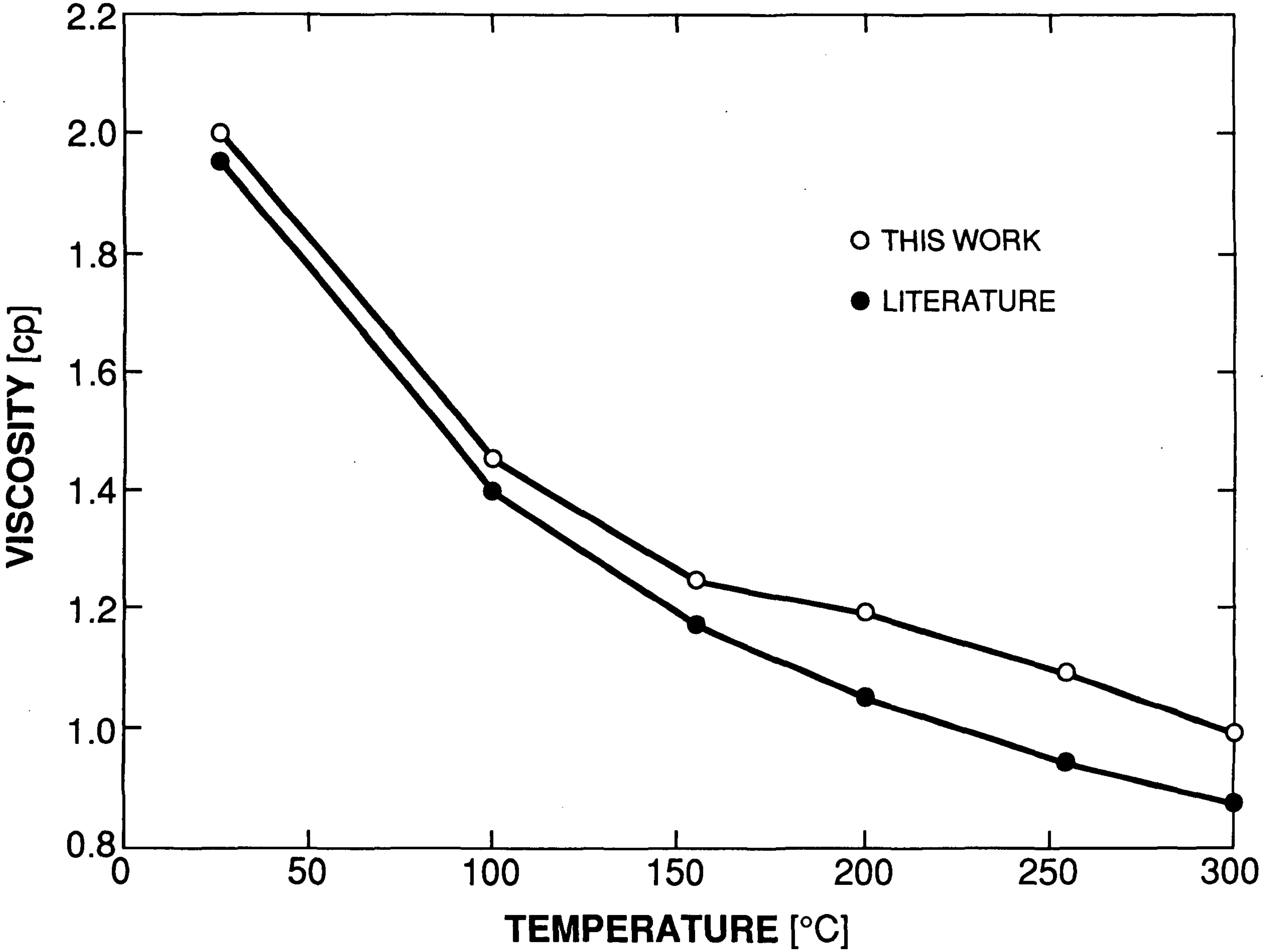

2.2
2.0
1.8
1.6
1.4
1.2
1.0
0.8
VISCOSITY [cp]
0
50
100
150
200
250
300
TEMPERATURE [°C]
○ THIS WORK
● LITERATURE

FIG. 9

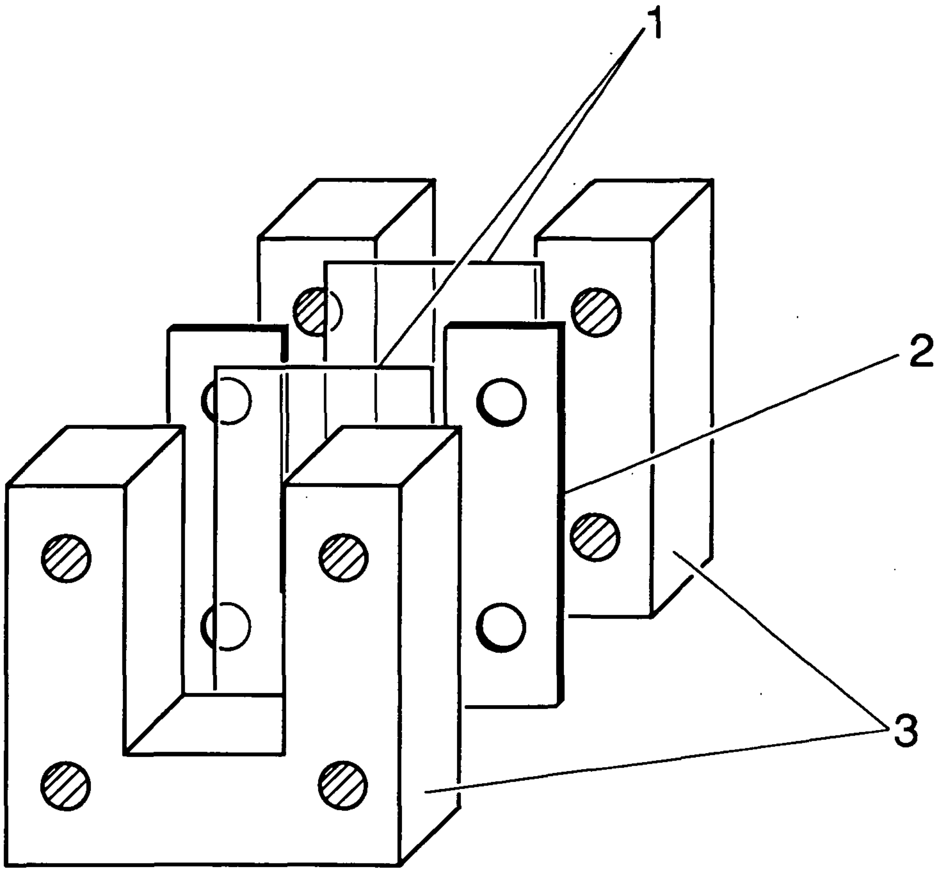

FIG. 10

RELATIONSHIP BETWEEN PHYSICAL AND COMPUTATIONAL DOMAINS

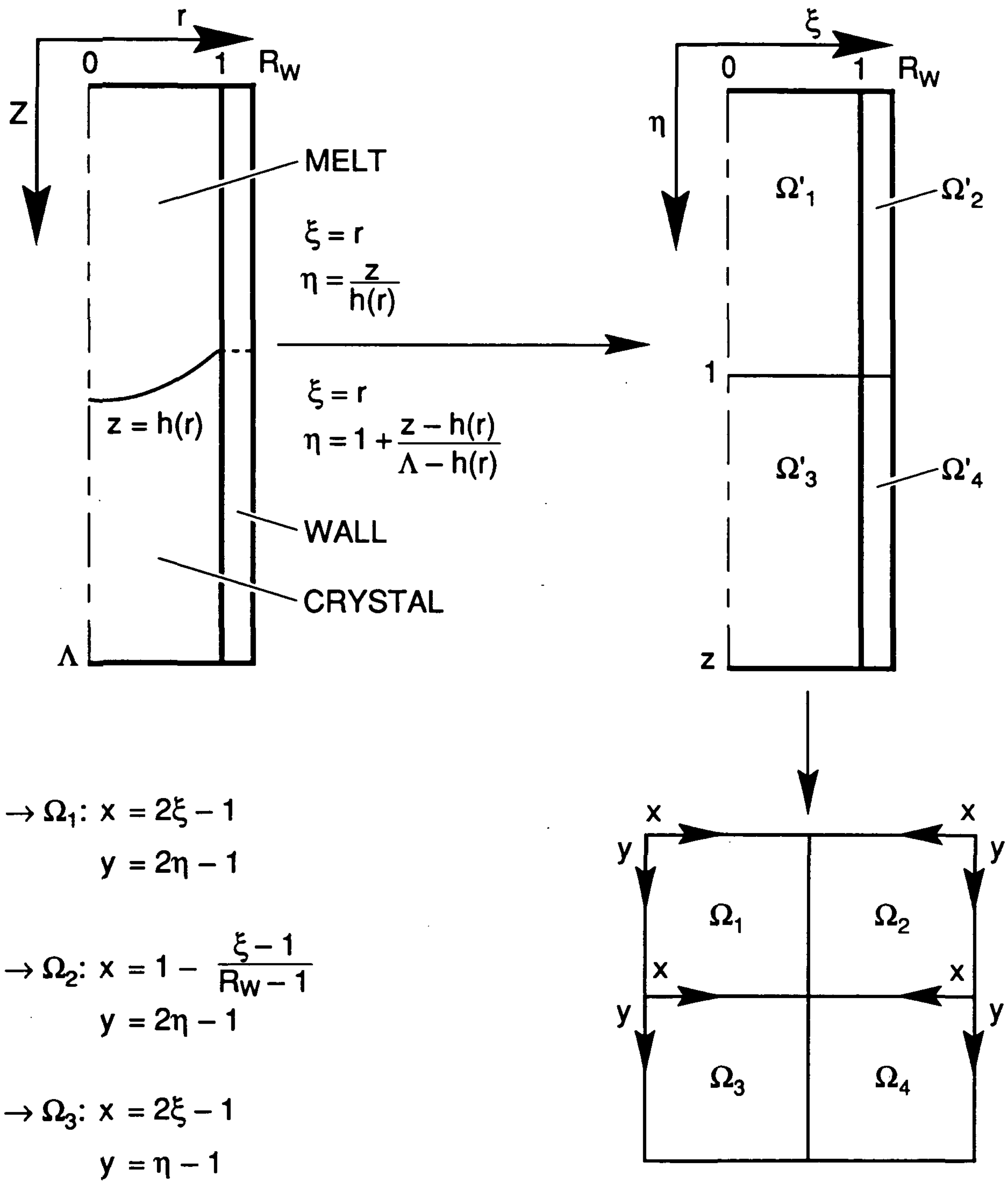

$$\xi = r$$
$$\eta = \frac{z}{h(r)}$$

$$\xi = r$$
$$\eta = 1 + \frac{z - h(r)}{\Lambda - h(r)}$$

$$\Omega'_1 \rightarrow \Omega_1:\ x = 2\xi - 1, \quad y = 2\eta - 1$$

$$\Omega'_2 \rightarrow \Omega_2:\ x = 1 - \frac{\xi - 1}{R_W - 1}, \quad y = 2\eta - 1$$

$$\Omega'_3 \rightarrow \Omega_3:\ x = 2\xi - 1, \quad y = \eta - 1$$

$$\Omega'_4 \rightarrow \Omega_4:\ x = 1 - \frac{\xi - 1}{R_W - 1}, \quad y = \eta - 1$$

For each Ω_i

$-1 \leq x \leq 1$
$-1 \leq y \leq 1$

FIG. 11

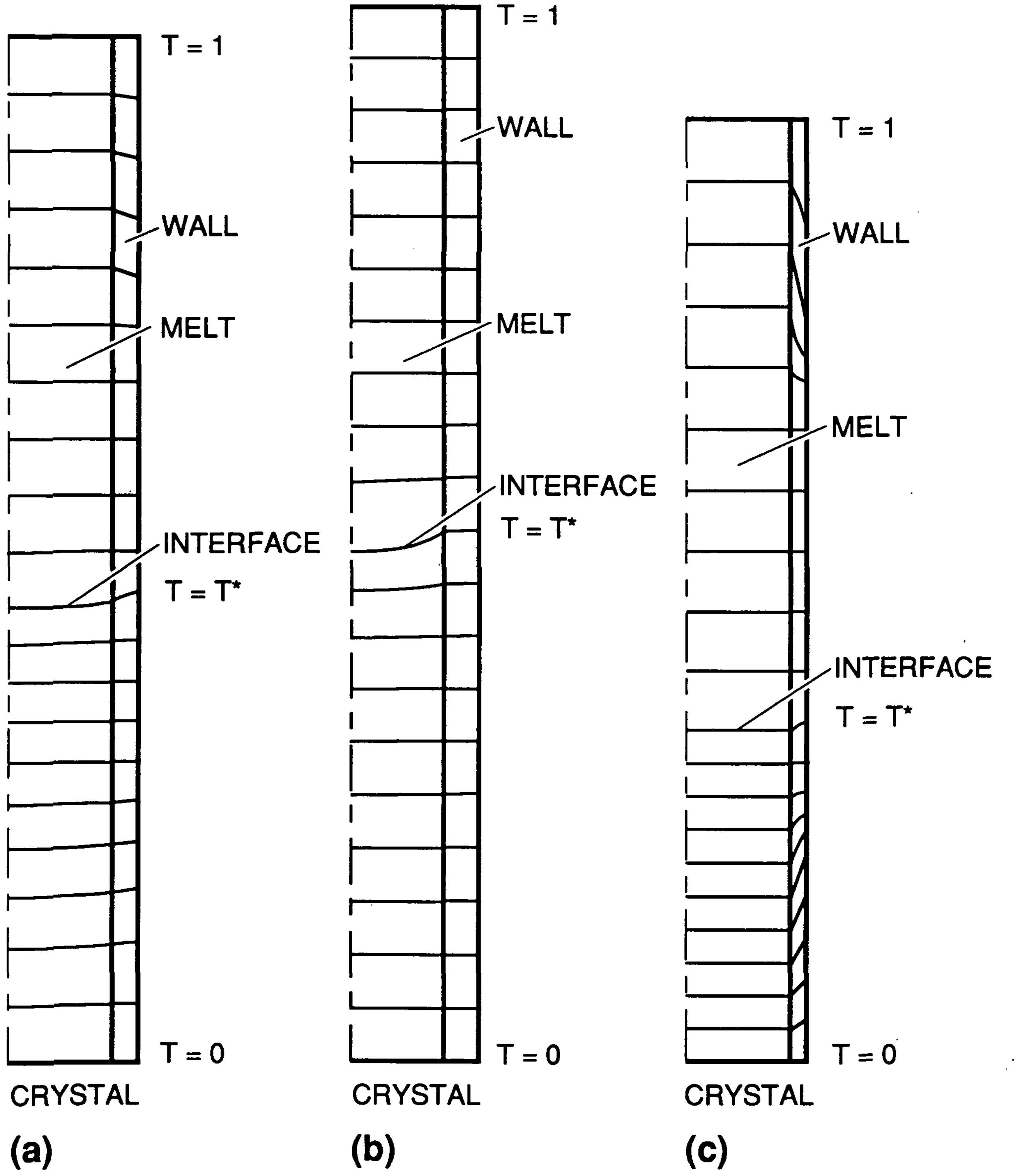
T = 1
WALL
MELT
INTERFACE
T = T*
T = 0
CRYSTAL
(a)
T = 1
WALL
MELT
INTERFACE
T = T*
T = 0
CRYSTAL
(b)
T = 1
WALL
MELT
INTERFACE
T = T*
T = 0
CRYSTAL
(c)

FIG. 12